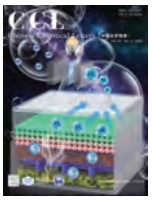
Chinese Chemical Letters 37 (2026) 111675

Contents lists available at ScienceDirect

Chinese Chemical Letters

journal homepage: www.elsevier.com/locate/cclet



Metal diborides as robust and highly stable electrodes for efficient electrocatalytic reduction of CO_2 to CO in ionic liquid-based electrolytes

Yidan Mao[a,1], Bingyu Li[a,1], Shuailing Ma[b,*], Siwen Cui[d], Zihan Zhang[e], Pinwen Zhu[d], Kongsheng Qi[a], Xiaodong Li[c], Weiwei Dong[c,*], Wei Luo[e], Rajeev Ahuja[e], Dexin Yang[a,*], Tian Cui[b,*]

[a] College of Chemistry, Zhengzhou University, Zhengzhou 450001, China
[b] Institute of High-Pressure Physics, School of Physical Scientific and Technology, Ningbo University, Ningbo 315211, China
[c] Beijing Synchrotron Radiation Facility (BSRF), Institute of High Energy Physics, Chinese Academy of Sciences, Beijing 100049, China
[d] Synergetic Extreme Condition High-Pressure Science Center, State Key Laboratory of Superhard Materials, College of Physics, Jilin University, Changchun 130012, China
[e] Condensed Matter Theory, Department of Physics and Astronomy, Uppsala University, Uppsala 75120, Sweden

ARTICLE INFO

Article history:
Received 8 March 2025
Revised 30 July 2025
Accepted 5 August 2025
Available online 6 August 2025

Keywords:
Metal diborides
Electrocatalytic reduction of CO_2
Ionic liquids
CO
Self-supporting electrodes

ABSTRACT

The electrocatalytic reduction of carbon dioxide (CO_2) into fuels holds significant promise for addressing energy and environmental challenges, albeit hindered by constraints in conversion efficiency, production rates, and electrode stability. Metal diborides are considered as promising electrocatalysts that may demonstrate superior CO_2 electroreduction performance due to their distinctive electronic properties. Herein, a series of novel bulk metal diborides, encompassing transition metals from group IVB to group VIIB elements, were fabricated using a high pressure-high temperature technique, which were directly utilized as self-supporting electrodes for electrocatalytic reduction of CO_2. The zirconium diboride (ZrB_2) electrode stood out in metal diborides with superior electrocatalytic activity in generating carbon monoxide (CO), achieving a Faradaic efficiency of 92.2% at −2.2 V *vs.* Ag/Ag^+ in ionic liquid-based electrolytes. Impressively, the ZrB_2 electrode demonstrated stable catalysis of CO_2 reduction to CO over a nearly 60-h electrolysis period. Furthermore, the ZrB_2 electrode and ionic liquid-based electrolytes could synergistically catalyze the reduction of CO_2 to CO. Experimental results and density functional theory calculations support the notion that exposed metal sites on the ZrB_2 (001) surface could enhance $^*CO$ desorption and restrain the hydrogen evolution reaction, thereby facilitating the conversion of CO_2 into CO.

© 2026 Published by Elsevier B.V. on behalf of Chinese Chemical Society and Institute of Materia Medica, Chinese Academy of Medical Sciences.

Since the Industrial Revolution, excessive carbon dioxide (CO_2) emissions have emerged as a significant concern due to their potential to exacerbate global warming, contribute to sea level rise, and harm ecosystems [1]. The conversion of CO_2 into high-value-added products through methods, such as electrocatalysis, photocatalysis, and thermal catalysis, represents an effective approach to utilize CO_2 resources and advance towards achieving carbon neutrality [2–4]. Electrocatalysis distinguishes itself among the aforementioned methods for its inherent simplicity, operability, and the ability to harness electricity generated from renewable resources [4,5]. However, the electrocatalytic reduction of CO_2 encounters significant thermodynamic barriers and slow reaction kinetics, especially during the conversion of the stable linear CO_2 molecule into the $^*CO_2^-$ radical anion [5]. Thus, the advancement of efficient and durable electrocatalysts with high current density and superior selectivity for desired production is essential for enhancing the kinetics of the CO_2 electroreduction.

Currently, numerous researchers are actively exploring the applications of non-precious transition metal-based electrocatalysts in the field of the CO_2 electroreduction, due to their abundant reserves and competitive catalytic performance [2,6–8]. As illustrated in Table S1 (Supporting information), various classes of transition metal compounds have been explored for the CO_2 electrore-

* Corresponding authors.
E-mail addresses: mashuailing@nbu.edu.cn (S. Ma), dongww@ihep.ac.cn (W. Dong), yangdx@zzu.edu.cn (D. Yang), cuitian@nbu.edu.cn (T. Cui).
[1] These authors contributed equally to this work.

https://doi.org/10.1016/j.cclet.2025.111675
1001-8417/© 2026 Published by Elsevier B.V. on behalf of Chinese Chemical Society and Institute of Materia Medica, Chinese Academy of Medical Sciences.

duction, including metal nitrides, sulfides, phosphides, and antimonides. These electrocatalysts have demonstrated good catalytic performance for the CO_2 electroreduction, with certain systems achieving remarkable Faradaic efficiencies exceeding 90 % for target products under optimized conditions. Despite these advances, metal borides remain relatively underexplored for the CO_2 electroreduction compared to other transition metal compounds. Recently, some researchers have discovered that incorporating trace B (<10 wt%) into metal structures as B-doped catalysts could result in a redistribution of electron states in metal electrocatalysts [9–14]. This change could alter the adsorption of reaction intermediates, thereby impacting the catalytic performance in the electrocatalytic reduction of CO_2 [15]. For example, introducing B atoms (2.3 wt%) into bismuth (Bi) could alter its local electronic structure, thereby enhancing the catalytic activity for CO_2 electroreduction and improving the selectivity for HCOOH over a wide potential range [16]. The intercalation of B atoms (1.26 wt%) could also adjust the average oxidation state of copper (Cu), control *CO adsorption and dimerization, and then promote the generation of C_2 products [17]. Moreover, a B-doped (6.3 at%) palladium catalyst (Pd-B/C) was more effective in boosting the formation of HCOOH compared to Pd/C [18]. These results indicated that the introduction of trace B element in metal structures could affect the activity and selectivity of electrocatalytic reduction of CO_2. Therefore, we speculate that transition metal borides with a precisely defined structure, higher B content and larger CO_2 adsorption capacity [19,20] hold great potential to serve as cost-effective and high-efficiency candidates for the electrocatalytic reduction of CO_2.

Notably, transition metal borides exhibit diverse composition, structural, and electronic characteristics, primarily including metal-rich borides (M_xB, $x > 1$), monoborides (MB), metal diborides (MB_2), and boron-rich borides (MB_x, $x > 2$) [21]. Among these borides, the well-known hexagonal AlB_2-type (*P6/mmm*) metal borides with high electrical conductivity and low electrical resistivity have attracted significant attention from researchers [22]. This kind of borides is characterized by close-packed transition metal sheets and graphene-like B layers, and can be synthesized with a variety of transition metals [23]. The presence of graphene-like B layers played an important role in enhancing electronic conductivity and providing more active sites [24]. It is worth noting that the choice of transition metals and the interaction between B and transition metals can have a profound effect on the physical and chemical properties of transition metal diborides, particularly in terms of their electrocatalytic performance [25]. Moreover, Li *et al*. theoretically demonstrated that monolayer two-dimensional transition-metal diborides exhibited a remarkable catalytic activity in selectively converting CO_2 to CH_4 [26]. Additionally, hard/superhard transition metal diborides obtained through the high pressure-high temperature (HPHT) are integral bulks, which can be directly utilized as self-supporting electrodes for electrocatalytic reduction of CO_2 [27]. In comparison to traditional powder electrocatalysts, these self-supporting electrodes can not only prevent the aggregation of electrocatalyst or the concealment of active sites caused by binder addition [28], but also eliminate the interface impedance between the conductive substrate and electrocatalyst. This facilitates efficient electron and proton transfer [29], which will ultimately enhance the catalytic performance for the electrocatalytic reduction of CO_2. The aforementioned facts motivate us to further explore the catalytic performance of various AlB_2-type metal borides self-supporting electrodes for the electrocatalytic reduction of CO_2.

In this study, the AlB_2-type metal diborides (TM = Ti, Zr, Hf, V, Nb, Ta, Cr, Mn, Mo) were fabricated using the HPHT method (Fig. 1a). The detailed temperature, pressure, and duration parameters for preparing different metal diborides are provided in Table S2 (Supporting information). The X-ray diffraction (XRD) patterns of different samples in Fig. 1b confirm the successful synthesis of the hexagonal AlB_2-type metal diborides. Meanwhile, it can also be seen that these transition metal diborides synthesized by the HPHT method exhibit high crystallinity and purity. As depicted in Fig. 1c, the Rietveld refinement of XRD pattern reveals that the ZrB_2 sample corresponds to a hexagonal unit cell with the space group *P6/mmm* (No. 191) [30]. The lattice parameters for the ZrB_2 sample are $a = b = 3.16067(3)$ and $c = 3.52094(6)$ (Table S3 in Supporting information), showing excellent agreement with values previously documented in the literature. Fig. 1d shows the comparison of average distance for adjacent metal-B and B-B atoms in different metal diborides. Although the average distances of metal-B and B-B may change with the variation of metal atoms, these metal diborides adapts the typical AlB_2-type structure characterized by graphene-like B layers sandwiched between transition metal layers (Fig. S1 in Supporting information). To further investigate the electronic structure of the ZrB_2 sample, the electronic characteristic was examined using electron localization function (ELF) and density of states (DOS). The ELF analysis (Fig. 1e) reveals that there are ionic Zr-B and covalent B-B bonds in the ZrB_2 sample. Meanwhile, DOS value is not zero at Fermi energy level for the ZrB_2 sample (Fig. 1f), indicating the intrinsic metallic behavior of the ZrB_2 sample. In addition, as confirmed by the DOS result (Fig. 1f), the metallic property of the ZrB_2 sample mainly originates from d electrons of Zr layers, which can enhance its catalytic activity.

The morphologies of various metal diborides were also measured by scanning electron microscopy (SEM). In Fig. S2 (Supporting information), it can be observed that the surfaces of the obtained bulk metal diborides exhibit a rough and irregular texture, resulting from the abrasion of diamond griding disk. Meanwhile, high-resolution SEM images (Fig. S3 in Supporting information) reveal that different metal diborides were all composed of tightly packed, irregular nanoblocks. To further explore the morphology and structure of metal diborides, we conducted transmission electron microscopy (TEM) and high-resolution TEM (HRTEM) tests using the ZrB_2 sample as an example. Combining high-resolution SEM (Fig. S3b) and TEM images (Fig. 2a), it can be observed that the ZrB_2 sample possesses a densely packed nano-block structure with grain size around 0.3–1.0 μm. In the HRTEM image (Fig. 2b) of the ZrB_2 sample, the interplanar spacings of 0.272 nm and 0.333 nm can be attributed to the (100) and (001) planes of ZrB_2 [31], respectively. The selected area electron diffraction (SAED) image (Fig. 2c) of the ZrB_2 sample corresponds to the (101) and (100) planes of the hexagonal ZrB_2 phase [32]. These findings are in agreement with the XRD results (Fig. 1b). The energy dispersive X-ray spectroscopy (EDS) mapping (Fig. 2d) of the ZrB_2 sample reveals a uniform distribution of the elements Zr (green) and B (red). A small amount of oxygen (O) elements is also observed on the surface of the ZrB_2 sample, which may be attributed to surface oxidation when exposed to air. To further investigate the chemical states of the elements in the ZrB_2 sample, X-ray photoelectron spectroscopy (XPS) spectra were analyzed, with the results shown in Figs. 2e and f, and Fig. S4 (Supporting information). The high-resolution XPS spectrum of Zr 3d (Fig. 2e) consists of four peaks. The binding energies at 178.7 eV (Zr $3d_{5/2}$) and 181.2 eV (Zr $3d_{3/2}$) correspond to Zr-B bonds in ZrB_2, while the other two peaks located at 183.0 eV (Zr $3d_{5/2}$) and 185.5 eV (Zr $3d_{3/2}$) are attributed to Zr-O bonds of ZrO_2 [31,33,34]. The B 1s XPS spectrum (Fig. 2f) can be resolved into two peaks. The peak at approximately 187.5 eV is assigned to B-Zr bonds in ZrB_2, while the peak at 187.9 eV belongs to B-B bonds [31,33,35]. In the O 1s spectrum (Fig. S4), the peak with a binding energy of 531.8 eV corresponds to O-Zr bonds in ZrO_2 [31,34], which may come from the surface oxidation of the ZrB_2 sample in air, consistent with the EDS mapping result (Fig. 2d). Moreover, XPS spectra of other metal diborides are presented in Figs. S5-S12 (Supporting information), respectively. The above

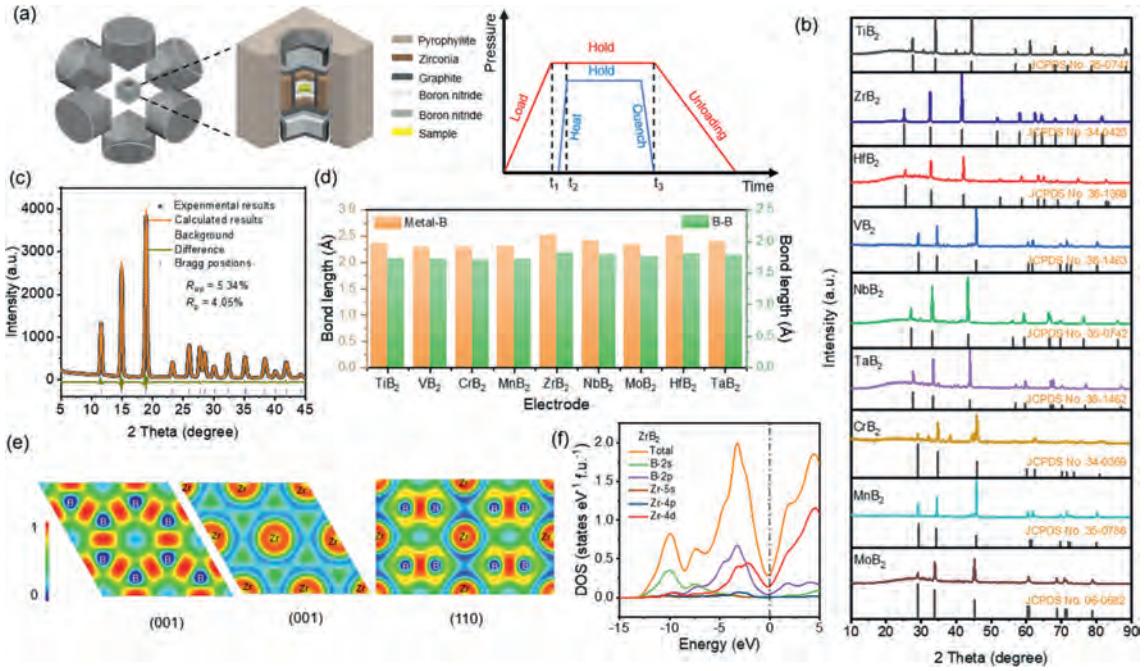


Fig. 1. (a) Schematic illustration of the HPHT method and procedure. (b) The XRD patterns of different metal diborides. (c) The Rietveld refinement of XRD pattern for the ZrB_2 sample. (d) The average distance of adjacent metal-B and B-B atoms in different metal diborides. (f) ELF of different planes for the ZrB_2 sample. (f) DOS of the ZrB_2 sample.

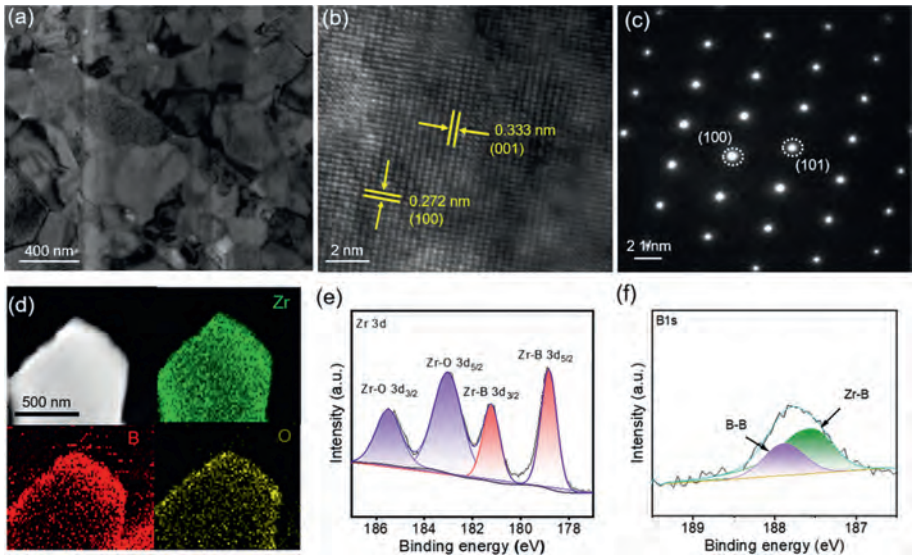


Fig. 2. The characterization results of the ZrB_2 sample: (a) TEM image, (b) HRTEM image, (c) SAED image, (d) EDS mapping images, (e) high-resolution XPS spectrum of Zr 3d, and (f) high-resolution XPS spectrum of B 1s.

results indicate highly quality AlB_2-type metal diborides bulks can be synthesized using the HPHT method, accompanied by slight surface oxidation when exposed to air. This distinctive structure confers special physical and chemical properties upon them, potentially enhancing their effectiveness in facilitating electrocatalytic reactions [36].

To assess the catalytic performance of as-synthesized metal diborides for the electrocatalytic reduction of CO_2, a series of electrochemical tests were conducted in a H-type cell employing a 1 mol/L [Bmim]PF_6-containing acetonitrile ([Bmim]PF_6(1M)-MeCN) solution as the electrolyte. In this study, the metal diborides, including TiB_2, ZrB_2, HfB_2, VB_2, NbB_2, TaB_2, CrB_2, MnB_2, and MoB_2, formed integral bulk materials, which were directly utilized as self-supporting electrodes for the electrocatalytic reduction of CO_2. The controlled potential electrolysis was initially carried out over different metal diborides at −2.2 V *vs.* Ag/Ag^+ in CO_2-saturated [Bmim]PF_6(1M)-MeCN electrolytes. The products were detected by gas chromatography (GC) and nuclear magnetic resonance (NMR) spectroscopy. Upon analysis, it was found that the main gaseous products on these metal diborides were CO and H_2, with no liquid products being generated (Fig. 3a). At −2.2 V *vs.* Ag/Ag^+, the ZrB_2 electrode exhibited a CO Faradaic efficiency of 92.2%, significantly outperforming other metal diborides. Meanwhile, the current densities of different electrodes were normalized according to their geometric surface areas. In Fig. 3a, the ZrB_2 electrode achieved a total current density of 51.5 mA/cm^2, which was 3.4, 3.4, 2.5, 2.1, 4.4, 4.7, 1.8, and 3.9 times higher than those of TiB_2, HfB_2, VB_2, NbB_2, TaB_2, CrB_2, MnB_2, and MoB_2 electrodes, respectively. These results

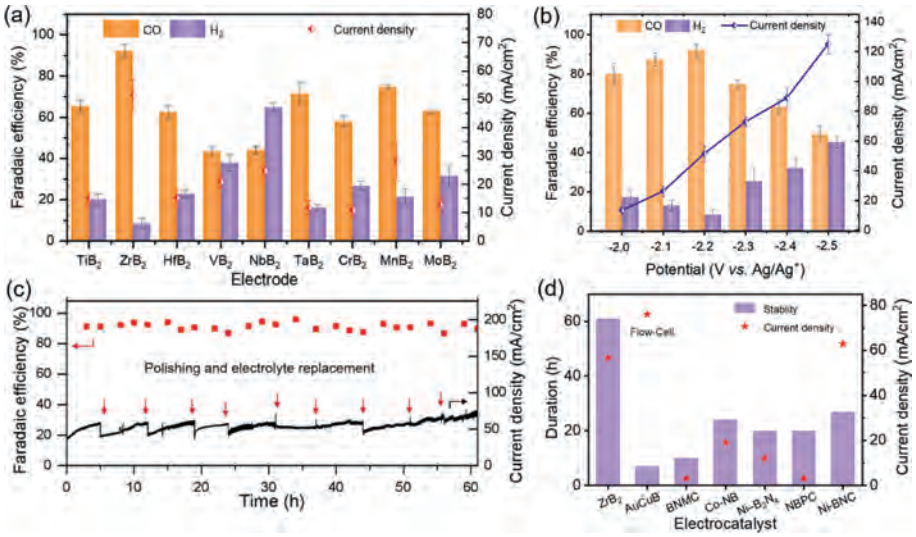


Fig. 3. (a) The current density and CO Faradaic efficiency on various metal diborides at −2.2 V *vs.* Ag/Ag^+. (b) The current density and CO Faradaic efficiency on the ZrB_2 electrode at different applied potentials. (c) Long-term stability of the ZrB_2 electrode in CO_2-saturated [Bmim]PF_6(1M)-MeCN electrolytes at −2.2 V *vs.* Ag/Ag^+. (d) The duration and current density of different B-containing electrocatalysts for the electrocatalytic reduction of CO_2 to CO [9–13].

suggest that the type of metal elements in the AlB_2-type metal diborides has a significant impact on the electrochemical reduction of CO_2 to CO. Meanwhile, linear sweep voltammetry (LSV) curves of the ZrB_2 electrode were recorded in Ar- or CO_2-saturated electrolytes (Fig. S13 in Supporting information), which indicated that the ZrB_2 electrode exhibits the ability to catalyze CO_2 reduction. In addition, to confirm the carbon source of CO product on the ZrB_2 electrode, the controlled potential electrolysis experiment was conducted under the same conditions, except that the CO_2 atmosphere was replaced with the Ar atmosphere. From Fig. S14 (Supporting information), it can be observed that no CO was detected under the Ar atmosphere, indicating that CO primarily originated from the reduction of CO_2. In a more comprehensive investigation, the relationship between the current density (or CO Faradaic efficiency) and the applied potential was analyzed for each metal diboride over a potential range from −2.0 V to −2.5 V *vs.* Ag/Ag^+ (Fig. 3b, Figs. S15 and S16 in Supporting information). When the applied potential was shifted negatively, the current densities over various metal diborides exhibited increasing trends (Fig. 3b and Fig. S15), and the Faradaic efficiencies of CO on different metal diborides followed volcano plots (Fig. 3b and Fig. S16). Impressively, the ZrB_2 electrode demonstrated an outstanding CO Faradaic efficiency of 92.2 % at a potential of −2.2 V *vs.* Ag/Ag^+, accompanied by a current density of 51.5 mA/cm^2 (Fig. 3b). As the applied potential decreased to values less than −2.2 V *vs.* Ag/Ag^+, the CO Faradaic efficiencies on the ZrB_2 electrode correspondingly diminished. As shown in Figs. S15 and S16, only the MnB_2 electrode achieved the maximum CO Faradaic efficiency (74.7 %) at −2.2 V *vs.* Ag/Ag^+, with corresponding current density of 34.9 mA/cm^2. The maximum CO selectivity at the surfaces of HfB_2 (72.0 %), VB_2 (61.2 %), NbB_2 (51.9 %), and CrB_2 (67.0 %) electrodes was observed at −2.3 V *vs.* Ag/Ag^+, with corresponding current densities of 49.5, 27.9, 43.5, and 27.7 mA/cm^2, respectively. Meanwhile, the highest CO Faradaic efficiencies on TiB_2, TaB_2, and MoB_2 electrodes were 72.6 %, 84.8 %, and 82.4 % at −2.4 V *vs.* Ag/Ag^+, respectively. Although all of these metal diborides had the ability to electrocatalytically convert CO_2 into CO, the ZrB_2 electrode can efficiently facilitate this conversion and achieve the highest CO Faradaic efficiency (92.2 %) at a relatively lower applied potential (−2.2 V *vs.* Ag/Ag^+) compared to other metal diborides, indicating that the ZrB_2 electrode was more favorable for the electrocatalytic reduction of CO_2 to CO.

To further investigate the practicality of the ZrB_2 electrode, we conducted long-term stability testing in [Bmim]PF_6(1M)-MeCN electrolytes at a potential of −2.2 V *vs.* Ag/Ag^+. Considering the volatilization of MeCN and the accumulation of carbonaceous compounds on the ZrB_2 electrode surface during the electrolysis experiment, the electrolyte was changed and the electrode surface was polished by diamond griding disk every 5–7 h. It is evident from Fig. 3c that the current density and CO Faradaic efficiency remained relatively stable over the 61-h electrolysis period. Combining the SEM image and XPS spectra of the used ZrB_2 electrode (Fig. S17 in Supporting information), we discovered the good stability of the ZrB_2 electrode in effectively catalyzing the electroreduction of CO_2 to CO over prolonged operational periods. Despite the relatively stable current density maintained over the 61-h electrolysis period, we observed minor fluctuations in the current density for the electrocatalytic reduction of CO_2 with the electrolysis time. These fluctuations might be linked to factors such as the replacement of the electrolyte and the polishing of the electrode surface. Furthermore, slight variations in the charge-transfer resistance (R_{ct}) of the ZrB_2 electrode before and after the CO_2 electrolysis, as revealed by electrochemical impedance spectroscopy (EIS) measurements, could also contribute to changes in the current density [37]. As shown in Fig. S18 (Supporting information), the ZrB_2 electrode demonstrated relatively low R_{ct} values both before and after CO_2 electrolysis. This suggested that the ZrB_2 electrode possessed favorable electronic transfer kinetics, thereby facilitating the electrocatalytic reduction of CO_2. Moreover, a slight decrease in the R_{ct} values of the ZrB_2 electrode was observed from 3.2 Ω pre-electrolysis to 2.2 Ω post-electrolysis conditions, indicating a minor reduction in R_{ct} values that could influence the electrocatalytic performance.

To better demonstrate the advantages of the self-supporting ZrB_2 electrode, we prepared a comparative ZrB_2 powder as a control sample. The ZrB_2 powder was drop-casted onto carbon paper to fabricate a conventional electrode, designated as the p-ZrB_2 electrode. In Fig. S19a (Supporting information), the current density and CO Faradaic efficiency of the p-ZrB_2 electrode were lower than those of the self-supporting ZrB_2 electrode across the entire potential range, primarily due to the adverse effects of the Nafion binder required for its preparation. The binder might not only induce aggregation of ZrB_2 particles but also block active sites, thereby impairing the electrocatalytic performance of the

CO_2 reduction. Moreover, the p-ZrB_2 electrode demonstrated limited stability (Fig. S19b in Supporting information), maintaining the CO Faradaic efficiency and current density for only 3 h, as the crushed ZrB_2 sample with relatively large particles tended to detach from the electrode surface during the electrolysis. Further EIS measurements (Fig. S19c in Supporting information) revealed that the superior performance of the self-supporting ZrB_2 electrode might correlate with its lower R_{ct} value, which facilitated faster electron transfer rates and consequently enhanced the CO_2 reduction process. To the best of our knowledge, the stability and current density for the efficient electrocatalytic reduction CO_2 to CO observed on the ZrB_2 electrode surpasses most recently reported state-of-the-art B-containing electrocatalysts (Fig. 3d and Table S4 in Supporting information) [9–13], which is beneficial for the industrial application and development of CO_2 electroreduction. Meanwhile, the performance of Zr-containing electrocatalysts for the electrocatalytic reduction of CO_2 is also shown in Table S5 (Supporting information). It can be observed that the primary product of these Zr-containing electrocatalysts for this reaction was mainly CO, with the exception of the bimetallic Cu-Zr electrocatalyst (ZrO_2/Cu-Cu_2O) [38], whose main product was ethylene (C_2H_4). Compared to Zr-containing electrocatalysts that produced CO, the ZrB_2 electrode exhibits superior electrocatalytic performance. In addition, the ZrB_2 electrode displayed better stability compared to the transition metal compounds reported in the literature (Table S1).

It is widely recognized that the composition of the electrolyte plays a significant role in regulating the catalytic activity and product distribution of the electrocatalytic reduction of CO_2. In this study, we first evaluated the catalytic performance of the ZrB_2 electrode in an aqueous solution with potassium bicarbonate ($KHCO_3$, 1 mol/L) as supporting electrolyte and a non-aqueous electrolyte, specifically an MeCN solution with a supporting electrolyte of tetrabutylammonium hexafluorophosphate ($TBAPF_6$(1M)-MeCN). In 1 mol/L $KHCO_3$ aqueous electrolyte, the ZrB_2 electrode exhibited almost no catalytic activity towards CO_2 reduction, with the main product being H_2. It can be seen in Fig. 4a that the Faradaic efficiency of H_2 over the ZrB_2 electrode was approximately 100.0 % at all applied potential. In contrast, the highest CO Faradaic efficiency for the ZrB_2 electrode was 64.1 % at −2.5 V *vs.* Ag/Ag^+ in $TBAPF_6$(1M)-MeCN electrolytes, with a current density of 11.7 mA/cm^2 (Fig. 4b). The high catalytic activity and selectivity of CO observed in the $TBAPF_6$(1M)-MeCN electrolyte compared to 1 mol/L $KHCO_3$ electrolyte suggest that the non-aqueous solution containing $TBAPF_6$ contributes to enhancing the catalytic performance of the ZrB_2 electrode. Based on this, we endeavored to utilize the ZrB_2 electrode in non-aqueous electrolytes to investigate its electrocatalytic performance for CO_2 reduction. In non-aqueous electrolytes, ionic liquids are commonly used as a supporting electrolyte for the electrocatalytic reduction of CO_2, especially those including imidazole cations. These ionic liquids can regulate the adsorption of CO_2 and its intermediates, thereby changing the catalytic activity of the electrode and achieving a co-catalytic effect [39,40]. Thus, the catalytic activity of the ZrB_2 electrode was further tested in MeCN solutions consisting of imidazole ionic liquids, including $[Bmim]PF_6$, 1–butyl–3-methylimidazolium perchlorate ($[Bmim]ClO_4$), 1–butyl–3-methylimidazolium acetate ([Bmim]OAc), 1–butyl–3-methylimidazolium nitrate ($[Bmim]NO_3$), and 1-ethyl-3-methylimidazolium hexafluorophosphate ($[Emim]PF_6$) (Fig. 4c). The LSV curves in Fig. S20 (Supporting information) show that the ZrB_2 electrode exhibited a higher catalytic activity for CO_2 electroreduction in the $[Bmim]PF_6$(1M)-MeCN electrolyte compared to electrolytes containing other ionic liquids. In Fig. 4c, the current densities and CO Faradaic efficiencies in $[Bmim]PF_6$(1M)-MeCN and $[Emim]PF_6$(1M)-MeCN electrolytes at −2.2 V *vs.* Ag/Ag^+ were higher than those in $TBAPF_6$(1M)-MeCN electrolyte, indicating that ionic liquids with imidazole cations in the electrolytes could promote the generation of CO. In the $[Emim]PF_6$(1M)-MeCN electrolyte, the CO Faradaic efficiency (88.7 %) and total current density (39.2 mA/cm^2) were notably lower than those in the $[Bmim]PF_6$(1M)-MeCN electrolyte. This discrepancy may be attributed to the cation variation in the ionic liquids, influencing the solubility of CO_2 and thus modulating the catalytic performance of the electrocatalytic reduction of CO_2 [41–43]. Furthermore, substituting the anions in the $[Bmim]PF_6$ with ClO_4^-, OAc^-, and NO_3^- resulted in decreased reaction kinetics and CO Faradaic efficiency on the ZrB_2 electrode. This result could be a consequence of these anions altering the properties of the electric double layer near the surface of the ZrB_2 electrode, thereby decreasing the rate of CO generation [44]. Meanwhile, the strong association between the PF_6^- anion and the CO_2 molecule can improve the solubility of CO_2. Based on the above results, it can be concluded that the supporting electrolyte $[Bmim]PF_6$ was beneficial for the electrocatalytic reduction of CO_2. The perfect combination of an MeCN solution with a supporting electrolyte of $[Bmim]PF_6$ and the ZrB_2 electrode may promote CO_2 adsorption, which is crucial for effective CO_2 electroreduction. Fig. 4d also displays the impact of varying concentrations of $[Bmim]PF_6$ in the electrolyte on the electrocatalytic activity for the CO_2 electroreduction reaction using the ZrB_2 electrode at −2.2 V *vs.* Ag/Ag^+. In the pure acetonitrile electrolyte, only trace amounts of CO were detected with negligible current density. This was due to the inherently low ionic conductivity of acetonitrile as a non-aqueous solvent, which severely limited charge transport and impeded the kinetics of the electrocatalytic reduction of CO_2. As $[Bmim]PF_6$ concentration increased (<1 mol/L), both current density and CO Faradaic efficiency showed progressive enhancement, attributable to improved solution conductivity through ionic dissociation ($[Bmim]^+$ and $[PF_6]^-$) and facilitated charge transfer processes. However, exceeding 1 mol/L of $[Bmim]PF_6$ in the electrolyte led to declining performance metrics,

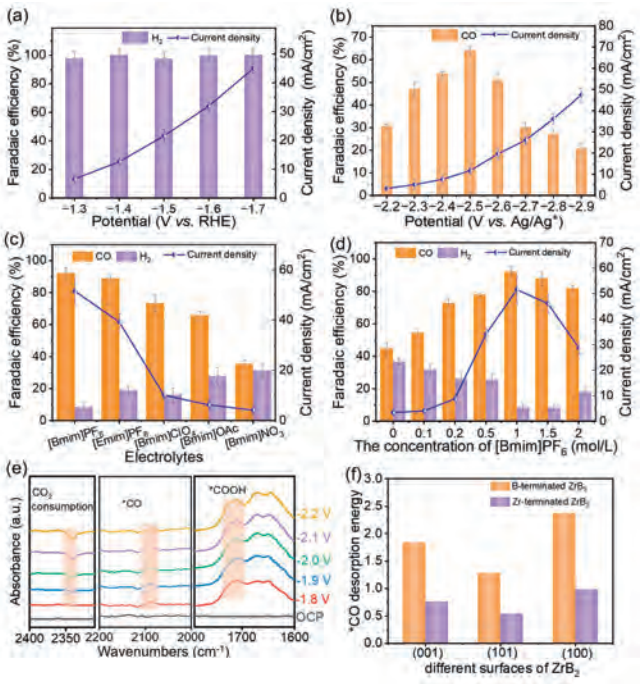


Fig. 4. The current density and CO Faradaic efficiency on the ZrB_2 electrode in different electrolytes: (a) 1 mol/L $KHCO_3$ aqueous solution, (b) $TBAPF_6$(1M)-MeCN electrolyte, (c) different ionic liquids(1M)-MeCN electrolyte, and (d) $[Bmim]PF_6$−MeCN electrolyte with varying concentrations of $[Bmim]PF_6$. (e) *In-situ* ATR-SEIRS spectra on the ZrB_2 electrode collected within the potential range of −1.8 V to −2.2 V *vs.* Ag/Ag^+. (f) The energy barriers for *CO desorption on different ZrB_2 surfaces.

primarily due to increased solution viscosity and intensified ion-pair ($[Bmim]^+$ and $[PF_6]^-$) interactions that collectively impeded mass transport and charge transfer kinetics. These observations established the optimal concentration of $[Bmim]PF_6$ was 1 mol/L, effectively enhancing the current density and CO Faradaic efficiency of the electrocatalytic CO_2 reduction.

In order to delve deeper into the potential reaction pathway for the electrocatalytic reduction of CO_2 to CO, *in-situ* attenuated total reflection surface-enhanced infrared reflection spectroscopy (ATR-SEIRS) was utilized to identify the reaction intermediates on the ZrB_2 electrode (Fig. 4e). The spectra were obtained within the potential range of −1.8 V to −2.2 V *vs.* Ag/Ag^+, using the measurement at open circuit potential (OCP) as the reference. It is noticeable that no vibration peak is observable in the spectra of the ZrB_2 electrode at OCP. In the potential range of −1.8 V to −2.2 V *vs.* Ag/Ag^+, newly emerged peaks at ∼1710 cm^{-1} could be assigned to the C=O stretching of the $^*COOH$ intermediate [45–49] during the electrocatalytic reduction of CO_2. Meanwhile, the peaks observed at ∼2090 cm^{-1} corresponded to $^*CO$ species, with their weak intensities possibly resulting from the rapid consumption of $^*CO$ for the formation of CO [50]. Moreover, the prominent characteristic peaks at ∼2345 cm^{-1} are attributed to the adsorbed CO_2 on the surface of the ZrB_2 electrode. As the applied potential decreased, the intensity of these peaks gradually strengthened, indicating an increase in the consumption of the adsorbed CO_2 [51]. Based on the above results, potential reaction pathway for the electrocatalytic reduction of CO_2 to CO on the ZrB_2 electrode can be speculated as follows: (1) $^* + CO_2 \rightarrow {}^*CO_2$; (2) $^*CO_2 + H^+ + e^- \rightarrow {}^*COOH$; (3) $^*COOH + H^+ + e^- \rightarrow {}^*CO$; (4) $^*CO \rightarrow {}^* + CO$, where * represents the adsorption site on the surface of the ZrB_2 electrode.

DFT calculations were also carried out to clarify the intrinsic activity for the electrocatalytic performance in CO_2 reduction on the ZrB_2 surface. The B-terminated ZrB_2 (001) and Zr-terminated ZrB_2 (001) were utilized as model electrocatalysts to explore the active sites of the ZrB_2 electrode for the electroreduction of CO_2 (Figs. S21 and S22 in Supporting information). In Fig. S23 (Supporting information), we found that the desorption of $^*CO$ is an endergonic process on both the B-terminated ZrB_2 (001) and Zr-terminated ZrB_2 (001) surfaces. Compared to the B-terminated ZrB_2 (001) model (1.84 eV), the Zr-terminated ZrB_2 (001) model exhibits a lower energy barrier for $^*CO$ desorption (0.76 eV) suggesting that metal edge sites of the ZrB_2 (001) surface can enhance $^*CO$ desorption, thereby promoting the formation of CO. To further validate the role of metal edge sites in the ZrB_2 electrode, the energy barriers for $^*CO$ desorption on the ZrB_2 (101) and ZrB_2 (100) surfaces, which can be observed in the XRD and TEM results (Figs. 1b, 2b and 2c), were also investigated. The results in Fig. 4f further demonstrate that the Zr-terminated ZrB_2 surface can facilitate $^*CO$ desorption compared to the B-terminated ZrB_2 surface, indicating that Zr sites in the ZrB_2 electrode are the primary active sites for the electrocatalytic reduction of CO_2 to CO. Moreover, the thermodynamic limiting potentials for the electrocatalytic reduction of CO_2 ($U_L(CO_2)$) and HER ($U_L(H_2)$) on the Zr-terminated ZrB_2 (001) are shown in Fig. S24a (Supporting information). The difference (ΔU_L) between $U_L(CO_2)$ and $U_L(H_2)$ is a positive value, which means a higher selectivity of the electrocatalytic reduction of CO_2 [52]. This is also consistent with experimental findings (Fig. 3b). These results indicate that the metal sites on the ZrB_2 (001) surface can lower the desorption energy of $^*CO$ intermediates, suppress the HER, and ultimately enhance the activity and selectivity for the electrocatalytic reduction of CO_2 to CO.

In conclusion, we have successfully developed a range of bulk metal diborides through the HPHT method, utilizing them as self-supporting electrodes for the electrocatalytic reduction of CO_2 in ionic liquid-based electrolytes. The as-obtained ZrB_2 electrode demonstrated outstanding electrocatalytic performance in the conversion of CO_2 to CO, achieving an impressive Faradaic efficiency for CO of up to 92.2 % at −2.2 V *vs.* Ag/Ag^+. More importantly, the ZrB_2 electrode also exhibited extraordinary stability, lasting up to ∼60 h. Mechanistic investigations corroborated that metal sites on the ZrB_2 (001) surface played multiple roles of facilitating the desorption of $^*CO$ intermediates, inhibiting the HER, thereby accelerating the formation of the CO product. The superior electrocatalytic performance of AlB_2-type metal borides positions them as highly promising candidates for CO_2 conversion applications, thereby likely to spur the progression and exploration of other metal borides in the field of CO_2 electroreduction.

Declaration of competing interest

The authors declare that they have no known competing financial interests or personal relationships that could have appeared to influence the work reported in this paper.

CRediT authorship contribution statement

Yidan Mao: Writing – original draft, Data curation, Investigation. **Bingyu Li:** Data curation, Investigation, Validation. **Shuailing Ma:** Methodology, Funding acquisition. **Siwen Cui:** Methodology, Investigation. **Zihan Zhang:** Data curation, Validation. **Pinwen Zhu:** Supervision, Funding acquisition. **Kongsheng Qi:** Formal analysis, Validation. **Xiaodong Li:** Supervision, Writing – review & editing. **Weiwei Dong:** Supervision, Writing – review & editing, Formal analysis, Funding acquisition. **Wei Luo:** Writing – review & editing, Funding acquisition. **Rajeev Ahuja:** Funding acquisition, Writing – review & editing. **Dexin Yang:** Writing – review & editing, Funding acquisition, Conceptualization, Supervision. **Tian Cui:** Supervision, Writing – review & editing, Funding acquisition.

Acknowledgments

The authors thank the National Natural Science Foundation of China (Nos. 22003058, 12204254), National Key Research and Development Program of China (No. 2023YFA1608902), the Program for Science and Technology Innovation Team in Zhejiang (No. 2021R01004) and the National Major Science Facility Synergetic Extreme Condition User Facility Achievement Transformation Platform Construction (No. 2021FGWCXNLJSKJ01). Wei Luo and Rajeev Ahuja thank Swedish Research Council (VR) (No. 2020–04410) for financial support.

Supplementary materials

Supplementary material associated with this article can be found, in the online version, at doi:10.1016/j.cclet.2025.111675.

References

[1] B. Ekwurzel, J. Boneham, M.W. Dalton, et al., Clim. Change 144 (2017) 579–590.
[2] D. Johnson, Z. Qiao, A. Djire, ACS Appl. Energy Mater. 4 (2021) 8661–8684.
[3] G. Xie, W. Guo, Z. Fang, et al., Angew. Chem. Int. Ed. 63 (2024) e202412568.
[4] M. Melchionna, P. Fornasiero, M. Prato, M. Bonchio, Energy Environ. Sci. 14 (2021) 5816–5833.
[5] S. Das, J. Pérez-Ramírez, J. Gong, et al., Chem. Soc. Rev. 49 (2020) 2937–3004.
[6] J. Zhu, Q. Zhang, C. Wang, et al., Nanoscale 17 (2025) 2709–2717.
[7] K. Lian, J. Ding, J. Zhang, et al., J. Mater. Chem. A 13 (2025) 2010–2018.
[8] S. Gao, H. Li, Z. Lu, et al., Carbon Energy 7 (2025) e637.
[9] Y. Liu, Y. Fang, Q. Yuan, J. Lu, H. Wang, Green Chem. 25 (2023) 1339–1344.
[10] X. Ma, J. Du, H. Sun, et al., Appl. Catal. B: Environ. 298 (2021) 120543.
[11] X. Song, W. Guo, X. Ma, et al., Green Chem. 24 (2022) 1488–1493.
[12] T. Shao, D. Duan, S. Liu, et al., Nanoscale 14 (2022) 833–841.
[13] C. Jia, W. Ren, X. Chen, W. Yang, C. Zhao, ACS Sustain. Chem. Eng. 8 (2020) 6003–6010.
[14] J. Song, X. Lei, J. Mu, et al., Small 19 (2023) 2305666.
[15] X. Liu, Y. Jiao, Y. Zheng, S.Z. Qiao, ACS Catal. 10 (2020) 1847–1854.
[16] D. Wu, R. Feng, C. Xu, et al., Nano-Micro Lett. 14 (2021) 38.
[17] Y. Zhou, F. Che, M. Liu, et al., Nat. Chem. 10 (2018) 974–980.

[18] B. Jiang, X.G. Zhang, K. Jiang, D.Y. Wu, W.B. Cai, J. Am. Chem. Soc. 140 (2018) 2880–2889.
[19] X. Lu, Y. Hu, S. Cao, et al., Phys. Chem. Chem. Phys. 25 (2023) 18952–18959.
[20] S.H. Mir, V.K. Yadav, J.K. Singh, ACS Appl. Mater. Interfaces 14 (2022) 29703–29710.
[21] H. Chen, X. Zou, Inorg. Chem. Front. 7 (2020) 2248–2264.
[22] F. Ling, K. Luo, L. Hao, et al., ACS Omega 5 (2020) 4620–4625.
[23] Z. Pu, T. Liu, G. Zhang, et al., Small Methods 5 (2021) 2100699.
[24] P.R. Jothi, Y. Zhang, K. Yubuta, et al., ACS Appl. Energy Mater. 2 (2018) 176–181.
[25] V. Mazánek, H. Nahdi, J. Luxa, Z. Sofer, M. Pumera, Nanoscale 10 (2018) 11544–11552.
[26] H. Yuan, Z. Li, J. Yang, J. Phys. Chem. C 123 (2019) 16294–16299.
[27] M. Wallace, High-pressure high-temperature (HPHT) synthesis of functional materials, in: S. Igor (Ed.), Sintering of Functional Materials, IntechOpen, Rijeka, 2017, pp. 166–182.
[28] B. Ren, H. Cui, C. Wang, Electrochem. Energy Rev. 5 (2022) 32.
[29] Y. Chen, Y. Yao, Y. Xia, et al., Nano Res. 13 (2020) 2777–2783.
[30] H. Li, L. Zhang, Q. Zeng, et al., Comp. Mater. Sci. 49 (2010) 814–819.
[31] C. Zhou, P. Wang, C. Wei, et al., J. Alloys Compd. 698 (2017) 27–32.
[32] P. Wang, Y. Qi, S. Zhou, et al., Phys. Status Solidi B 253 (2016) 1590.
[33] L. Scatteia, R. Borrelli, G. Cosentino, et al., J. Spacecr. Rockets 43 (2006) 1004–1012.
[34] S.H. Lee, Y. Sakka, Y. Kagawa, J. Am. Ceram. Soc. 91 (2008) 1715–1717.
[35] Y. Panayiotatos, Diam. Relat. Mater. 12 (2003) 1151–1156.
[36] F. Guo, Y. Wu, H. Chen, et al., Energy Environ. Sci. 12 (2019) 684–692.
[37] B. Qin, Y. Li, H. Wang, et al., Nano Energy 60 (2019) 43–51.
[38] P.P. Guo, Z.H. He, S.Y. Yang, et al., Green Chem. 24 (2022) 1527–1533.
[39] D. Yang, Q. Zhu, B. Han, The Innovation 1 (2020) 100016.
[40] X. Tan, X. Sun, B. Han, Natl. Sci. Rev. 9 (2022) nwab022.
[41] B.A. Rosen, A. Salehi-Khojin, M.R. Thorson, et al., Science 334 (2011) 643–644.
[42] C. Cadena, J.L. Anthony, J.K. Shah, et al., J. Am. Chem. Soc 126 (2004) 5300–5308.
[43] G. Hong, J. Jacquemin, P. Husson, et al., Ind. Eng. Chem. Res. 45 (2006) 8180–8188.
[44] D. Faggion, W.D.G. Gonçalves, J. Dupont, Front. Chem. 7 (2019) 1–8.
[45] J. Pei, T. Wang, R. Sui, et al., Energy Environ. Sci. 14 (2021) 3019–3028.
[46] B. Ratschmeier, B. Braunschweig, J. Phys. Chem. C 125 (2021) 16498–16507.
[47] N.J. Firet, W.A. Smith, ACS Catal. 7 (2016) 606–612.
[48] Y. Katayama, F. Nattino, L. Giordano, et al., J. Phys. Chem. C 123 (2018) 5951–5963.
[49] H. Chang, F. Gao, A. Luo, et al., Chem. Commun. 59 (2023) 7647–7650.
[50] K. Yao, J. Li, H. Wang, et al., J. Am. Chem. Soc. 144 (2022) 14005–14011.
[51] M. Dai, W. Ni, Z. Zeng, et al., Energy Environ. Sci. 17 (2024) 1531–1539.
[52] X. Li, W. Bi, M. Chen, et al., J. Am. Chem. Soc. 139 (2017) 14889–14892.